PHYSICAL REVIEW RESEARCH **4**, L012019 (2022)

Letter

Universality of breath figures on two-dimensional surfaces: An experimental study

L. Stricker,[1] F. Grillo,[2] E. A. Marquez,[3] G. Panzarasa,[4] K. Smith-Mannschott,[5] and J. Vollmer[6]
[1]*ETH Zürich, Department of Materials, Soft Materials, 8093 Zurich, Switzerland*
[2]*ETH Zürich, Department of Materials, Soft Materials and Interfaces, 8093 Zurich, Switzerland*
[3]*KU Leuven, Department of Chemistry, 3001 Leuven, Belgium*
[4]*ETH Zürich, Institute of Building Materials, Wood Materials Science, 8093 Zurich, Switzerland*
[5]*ETH Zürich, Department of Materials, Soft and Living Materials, 8093 Zurich, Switzerland*
[6]*University of Leipzig, Institute of Theoretical Physics, 04103 Leipzig, Germany*

(Received 3 September 2020; accepted 24 January 2022; published 16 February 2022)

Droplet condensation on surfaces produces patterns, called breath figures. Their evolution into self-similar structures is a classical example of self-organization. It is described by a scaling theory with scaling functions whose universality has recently been challenged by numerical work. Here, we provide thorough experimental testing, where we inspect substrates with vastly different chemical properties, stiffness, and condensation rates. We critically survey the size distributions and the related time-asymptotic scaling of droplet number and surface coverage. In the time-asymptotic regime, they admit a data collapse: the data for all substrates and condensation rates lie on universal scaling functions.

DOI: 10.1103/PhysRevResearch.4.L012019

Breath figures are droplets patterns formed by a supersaturated vapour flux condensing on a substrate [1]. They appear in nature, for example when dew deposits on leaves, spider nets and vegetable fibers. They also have an appealing potential for technological purposes. Possible applications include dew harvesting devices for water collection [2–4], heat exchangers with increased efficiency [5–8], and patterned surfaces production [9–13]. Breath figure self-assembly has been exploited to fabricate porous bead-on-string fibers [13]. Droplets have been used as a template to produce ordered porous materials for membrane manufacturing [14], as well as to introduce desired materials inside textiles by means of three-dimensional porous microstructures [15]. Recent studies have shown that droplet patterns on surfaces can also give origin to structural colors [16]. In all these applications, understanding the droplet formation process and the evolution of the condensation patterns is a crucial step towards controllability and further technological development.

The theory of breath figures is based on scaling arguments [17–22]. The condensation process leading to the formation of a droplet pattern develops in several phases [23], corresponding to different time and length scales characterizing the phenomenon. A first nucleation of droplets (primary nucleation) is followed by their initial growth as a monodisperse population. After some time, the droplets start to merge, releasing space on the substrate, which is used for further nucleation (secondary nucleation). The distribution continues to evolve, becoming polydisperse and eventually self-similar [17,18,24,25]. Scaling concepts, closely related to fractals theory, can be used to describe the evolution of the droplet distribution [25,26]. Experiments [17,26–29] and simulations [19,26,30,31] have shown that, in the late-time regime, the droplet size distribution is bimodal, with two well-separated parts. In particular, it features a bell-shaped peak, corresponding to the monodisperse population of the largest hence oldest droplets, and a power law distribution of smaller droplets, which is terminated by a cutoff function at the nucleation length scale. Scaling manifests itself in a data collapse of droplet distributions taken at different times, and in the time dependence of the moments of the distribution. In the long-time regime, they approach power laws with exponents that can be expressed in terms of a single nontrivial exponent, denoted as “polydispersity exponent τ.” In particular, the asymptotic time decay of the droplet number and the porosity (ratio between nonwetted area and total substrate area) are described by the same exponent. It was widely expected that the polydispersity exponent is a universal number, depending only on the dimensionality of the system [17–22,32,33]. Its value was calculated [33] by assuming universality [34]. However, the exponents found in recent numerical simulations [26,31] differ clearly from the prediction. This calls for experimental studies. So far experimental studies have mostly addressed the early stages of the droplet nucleation [23,27,35], and the initial phases of the polydisperse transient regime [36,37], with noticeable exceptions in [8,26]. The impact of surface properties and condensation rates has not been examined.

Here, we present extensive experimental data for breath figures on a range of substrates with different stiffness, surface chemistry, and temperature. The different regimes of surface coverage are discussed with an emphasis on the self-similar phase. We observe the predicted scaling and critically survey

---

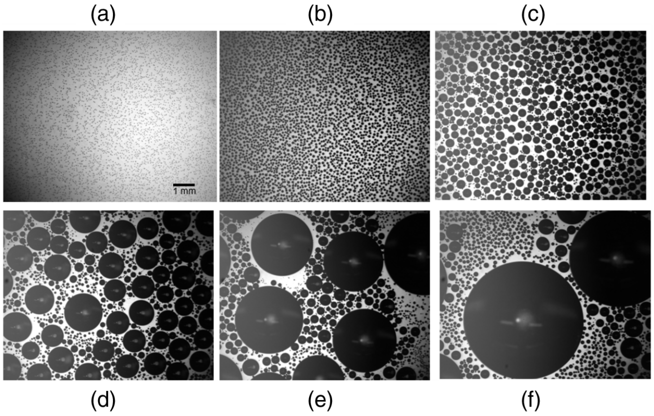

FIG. 1. Time evolution of the droplets condensation pattern on a silicone substrate with elastic modulus $E = 2$ MPa. Images are taken (a) 1 sec, (b) 10 sec, (c) 100 sec, (d) 15 min, (e) 250 min, and (f) 300 min after the beginning of the condensation process.

the predicted data collapse for all data of all experimental settings. The conclusion, that there are universal scaling functions, is substantiated by kinetic Monte Carlo simulations.

Evolution of droplet patterns. We induce the nucleation and growth of water droplets on substrates consisting of a glass cover slip either coated with a 30 μm layer of silicone (Dow Corning Sylgard 184) or silanized with tridecafluoro–1,1,2,2–tetrahydrooctyl trichlorosilane ($SiHCl_3$) or hexametildisilazane (HMDS). The upper side of the substrates is exposed to a steady flux of air saturated with water at room temperature. On the bottom, they are in contact with a temperature-controlled plate at a set-point temperature T_p^* of 5 °C. We image the droplets from the top with a dissecting microscope (Nikon SMZ80N). The smallest measured droplets have a radius of about 15 μm, the largest about 2.5 mm. In each image, we identify the center and radius of each droplet. We acquire images of the droplets over logarithmically spaced time intervals between 0.1 sec and 10 h, from the moment the first visually resolvable droplets appear. Using silicone substrates allows us to reduce the stiffness, and hence the number of nucleation sites respect to glass [38]. The static contact angle θ_c is measured via side imaging, with a CMOS camera (Thorlabs, DCC3240M) and LED back-illumination, with a precision of 2°. On all substrates droplets can be considered hemispherical ($\theta_c \sim 90°$) except on HMDS-glass ($\theta_c = 67°$). Full details on the experimental setup, data acquisition, and analysis are given in Secs. A– C of Ref. [39].

Representative snapshots of droplet nucleation, growth, and coalescence on a silicone substrate with elastic modulus $E = 2$ MPa are shown in Fig. 1. After an initial burst of nucleation [Fig. 1(a)], the droplets grow with roughly uniform size [Fig. 1(b)] . After about one minute, the droplets start to come into contact and coalesce [Fig. 1(c)]. New droplets nucleate in the gaps between larger ones, and the range of droplet sizes grows [Figs. 1(d)–1(f)].

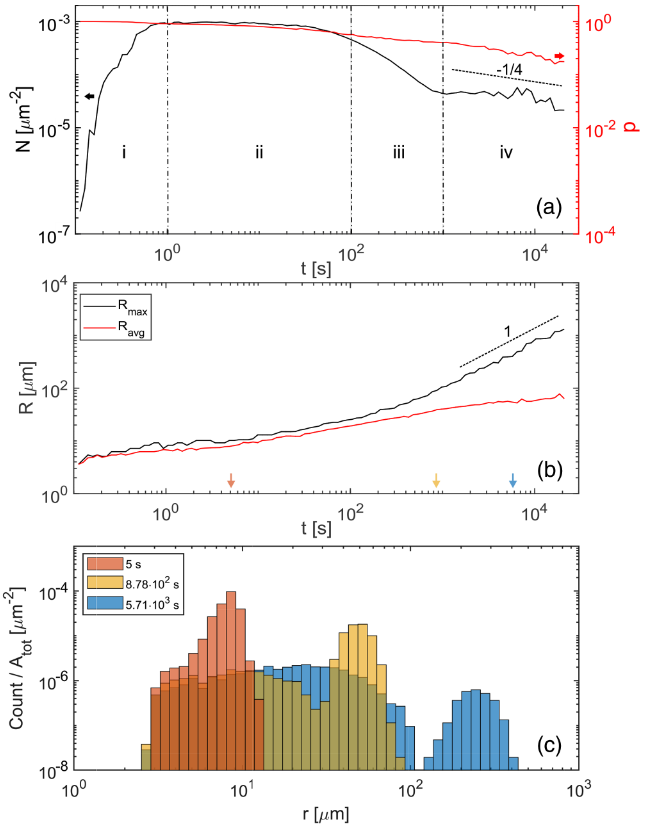

FIG. 2. Stages of growth. (a) Time evolution of the number of droplets per unit area (black, left vertical axis) and porosity (grey, red online, right vertical axis). (b) Time evolution of the maximum (black) and average (grey, red online) radius of a droplets population condensing on a silicone substrate ($E = 1$ MPa). (c) Frequency histograms of the radii r of the droplet population at different times: 1 (red), 15 (yellow), and 95 min (blue) from the beginning of the condensation process.

Four stages of the condensation process emerge clearly when we plot the total number of droplets per unit area as a function of time, $N(t)$, as shown in Fig. 2(a) (black line, left vertical axis). The nucleation stage lasts for the first second. It is characterized by a rapid increase in the number of droplets and it is labeled (i) in Fig. 2(a). In the uniform growth stage, labeled (ii) in Fig. 2(a), the number of droplets remains essentially fixed and the mean and maximum droplet radii increase, as shown in Fig. 2(b). Throughout the nucleation and growth stages, the droplet size distribution remains unimodal, as shown by the red histogram in Fig. 2(c). In the early coalescence stage, labeled (iii), the number of droplets per unit area steadily decreases [Fig. 2(a)], the droplets growth accelerates, as shown in Fig. 2(b), and the size distribution becomes bimodal, as shown by the yellow histogram in Fig. 2(c). In the late coalescence stage, starting after about 10^3 sec, labeled (iv), the number of droplets decays more slowly than before [Fig. 2(a)], while the spread between the maximum and mean droplet radii widens, as shown in Fig. 2(b), reflecting the broadening of the underlying size distribution [Fig. 2(c), blue histogram). As the droplets distribution grows, the free area on the substrate decreases. This decay is quantified by the porosity,

$$p(t) = 1 - \sum_i \frac{A_i(t)}{A_{\rm tot}}, \tag{1}$$

where the index i labels the ith droplet, $A_i = \pi R_i^2$ is its wetted area, with R_i its time-dependent radius, and $A_{\rm tot}$ is the

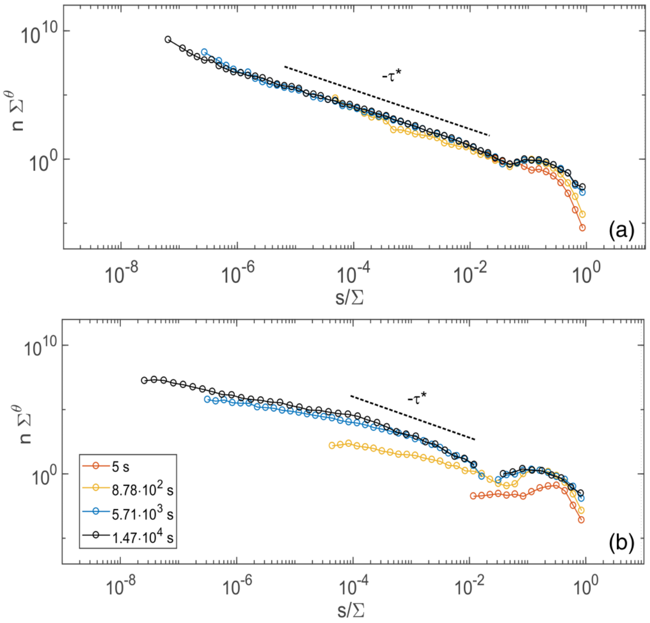

FIG. 3. Rescaled droplet number density as a function of the size s/Σ, where $s = r^3$, $\Sigma = \max s$ and $\theta = 5/3$ (a) from simulations and (b) from experiments, at different times, indicated in the legend. The dashed lines represent the theoretical prediction for the polydispersity exponent $\tau^\star = 19/12$.

total substrate area.[1] Experimentally, the porosity is calculated from the droplet coordinates and radii. Prior to the nucleation of droplets, for an empty surface, the porosity is equal to one. As the area covered by droplets grows in time, the porosity decays, as shown in Fig. 2(a) (grey line, red online, right vertical axis).

Scaling of the droplet number density. We now evaluate the droplet size distributions. The probability density function $n(s, t)$ represents the number of droplets of size s per substrate unit area, per unit size. The "size," proportional to the droplets mass, is defined as $s = r^3$, where r is the radius and n has units of m^{-5}. During the late-stage scaling regime, n should adopt a scaling form. In particular, it is expected [18,19] that the intermediate portion of the distribution, excluding the tails of the smallest and the largest droplets, scales as $n(s,t) \sim [s/\Sigma(t)]^{-\tau}\Sigma(t)^{-\theta}$, where θ is a trivial exponent, depending on the dimensionality of the system, τ is the polydispersity exponent and $\Sigma(t)$ is the maximum droplet size at time t. The exponent θ must take the value $5/3$ for three-dimensional droplets on a two-dimensional substrate, such that the dimensions of n and the scaling expression match. The exponent τ is expected to take a value of $19/12$ [33]. The resulting power laws are indicated by dashed lines in the plots of our data. Further discussion is provided in Sec. E of Ref. [39]. We analyze n both for experiments and simulations. In particular, we perform kinetic Monte Carlo simulations [40–43] on a 1200×1200 square lattice with periodic boundary conditions and a constant water flux impinging onto the surface. The simulations account for droplet nucleation and growth as well as for merging events. A full description is provided in Sec. I of Ref. [39].

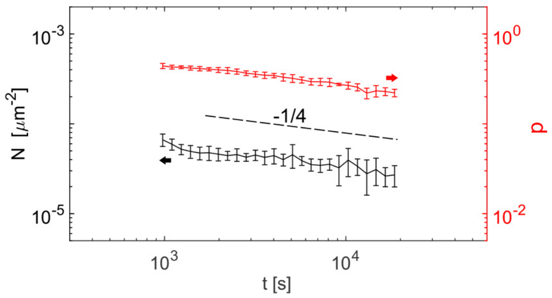

FIG. 4. Late-time evolution of porosity (grey, red online, right vertical axis) and number of droplets per unit area (black, left vertical axis), averaged over six experiments. The error bars represent the standard deviation.

To compare our findings to the theoretical predictions, we plot the rescaled droplet number density, $n(s,t)\Sigma^\theta$, in Fig. 3. In this plot, the droplet sizes are normalized by the maximum droplet size observed at that time point, $\Sigma(t)$. Thus, large droplet peaks line up at $s/\Sigma \approx 1$ for all times. As time progresses, the small droplet peak becomes broader and has a maximum value close to the smallest resolvable size.

At large times, the distribution presents three distinct features: an intermediate self-similar range where $n \sim (s/\Sigma)^{-\tau}$, a monodisperse bump describing the large droplets, and a tail describing the small droplets. Such features clearly appear in both our numerical and experimental results (Fig. 3). For all data, the large-droplet cutoff emerges for $s/\Sigma \gtrsim 10^{-2}$. The simulations show a power law over around four decades, in the intermediate scaling range, for $10^{-6} < s/\Sigma < 10^{-2}$. In contrast, for the experimental data, the scaling range is limited to at most two decades, $10^{-4} < s/\Sigma < 10^{-2}$, even for our latest time $t = 1.47 \times 10^4$ sec. The small-droplet cutoff is much broader for the experiments and it covers roughly three decades, with the cross-over at $s/\Sigma \approx 10^{-4}$. The experiments cannot be further extended in time, since gravitational effects impact the droplet shape when the large droplets approach the capillary length, $\sqrt{\gamma/\rho g} \approx 2.6$ mm.

Porosity and droplet number. The scaling form of the distribution entails that the porosity and the droplet number exhibit a power-law decay [18,19]. According to the theory, in the scaling regime, the radius of the largest droplets should scale as $R \sim t^\nu$ with exponent $\nu = 1$, and both the number of droplet per unit surface N, and the porosity p should evolve as a power law $N \sim p \sim t^{-k}$ [18,19], with exponent

$$k = 3\nu(\theta - \tau). \tag{2}$$

The derivations are provided in Sec. F– H of Ref. [39]. For $\theta = 5/3$ and Blackman's prediction $\tau = \tau^* = 19/12$ [33], we expect that $k = k^* = 1/4$, where the asterisks denote the specific theoretical values.

The temporal growth of the maximum droplet radius is shown in Fig. 2(b). In the last time decade of the experiment, it follows the predicted power law with exponent $\nu = 1$. Figure 4 shows the average of the porosity (grey, red online,

---

[1] Note that the porosity is an instantaneous measure of the area not covered by droplets at a certain time, thus, it differs from the "visited area" [44], which is the area that has been occupied by droplets at any previous time.

right vertical axis) and number of droplets per unit area (black, left vertical axis) averaged over 6 experiments. The error bars represent the standard deviation at each instant. Within the error bars, the decay rate of both the porosity and droplets number are compatible with the theoretical exponent $-1/4$ (dashed line), but deviations up to 20% remain possible [31,33]. Note that the exponent k is extremely sensitive to any variation of the exponent τ. A deviation $\Delta\tau$ from the theoretical prediction τ^*, would be enhanced by a factor of three in the deviation from k^*, thus resulting in a twentyfold increase of relative deviations, $\Delta k/k^* = 3\Delta\tau/(1/4) = 12\tau^*\Delta\tau/\tau^* = 19\Delta\tau/\tau^*$. Moreover, the integral quantities of porosity and droplet number are easier to evaluate than the full droplet distribution.

Condensation for different surfaces and water fluxes. In view of its robust scaling in the late time regime, we now use the porosity time decay to compare condensation for different surfaces and condensation fluxes. For the porosity, the theory predicts that

$$p(t) = \left(\frac{s_p}{x_p\,\Sigma(t)}\right)^{\theta-\tau} \quad \text{with} \quad \Sigma(t) = R_{\max}^3 = \left(\frac{\pi\Phi}{3\alpha}t\right)^3. \tag{3}$$

Here, Φ is the constant water flux, i.e., the water volume deposited on the substrate per unit surface per unit time, $\alpha = (\pi/3)(2+\cos\theta_c)(1-\cos\theta_c)^2/(\sin\theta_c)^3$ is a geometrical factor accounting for the contact angle θ_c, measured through the liquid phase, $s_p/x_p\Sigma(t)$ is the width of the scale separation between smallest and largest droplets; the nondimensional sizes $s_p/\Sigma(t)$ and x_p, where s_p and x_p are constants, represent indeed the cutoffs for small and large droplets, respectively. Full details are provided in Sec. G of Ref. [39]. For this discussion, we note that, due to the small exponent $\theta - \tau = 1/12$, the ratio $(s_p/x_p)^{\theta-\tau}$ in Eq. (3) can change by at most 30%, even for s_p/x_p differing by two orders of magnitude for two vastly different materials. Hence, it remains practically unvaried, and the impact of Φ/α on the time evolution of $\Sigma(t)$ is expected to be the only noticeable parameter influencing the asymptotic evolution of the porosity.

Figure 5(a) shows the time evolution of the porosity for three different surfaces with the same temperature of the cooling plate, $T_p^* = 5\,^\circ$C, and the same contact angle up to experimental precision. The light and dark grey curves (red and blue online) correspond to 1 and 2 MPa silicone surfaces, respectively, while the black curve shows the porosity for fluor-silane coated glass. The two silicone surfaces behave similarly, with a monotonic decrease in the porosity. However, the softer surface ($E = 1$ MPa) is populated at a slower rate. Hence the drop in porosity occurs later, as one can observe for times around 100 s. The silanized glass surface behaves very differently in the early stages of condensation. It has a very high nucleation rate and is covered by tiny droplets almost immediately, such that the porosity drops to a very small value. Initially, the droplets are so small and so densely packed that they cannot be individually resolved (Fig. S5 in Ref. [39]). Between 10 and 100 s, the droplets start to merge such that the areas in between can be discerned, and the porosity rises towards the values observed for the silicone surfaces. In the late-time scaling regime, the surface is entirely covered by water droplets, and the flux Φ onto the droplets is solely determined by the cooling plate temperature, such that Eq. (3) predicts the same power law for the three systems. Despite dramatic difference in initial droplet nucleation and growth, at late times, $t \gtrsim 1000$ s, all data fall exactly on top of each other. The three surfaces do not only share the same scaling exponent, but also the same prefactor of the power law.

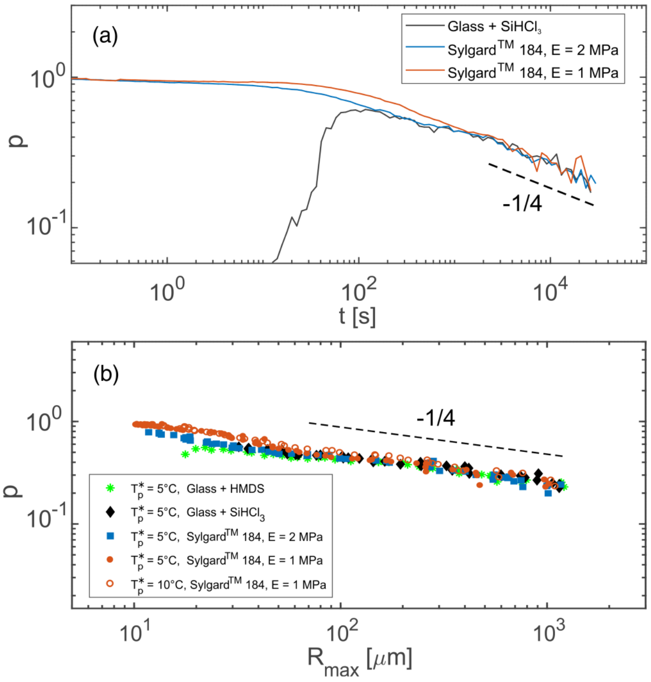

FIG. 5. Evolution of porosity (a) as a function of time for different rigid surfaces with $T_p^* = 5\,^\circ$C: fluor-silanized glass (black) and silicone with $E = 2$ MPa (dark grey, blue online) and $E = 1$ MPa (light grey, red online) (b) as a function of maximum droplet radius, for different contact angles θ_c and vapour fluxes, regulated by changing the plate temperature T_p^*. The substrates are HDMS-silanized glass ($\theta_c = 67^\circ$) with $T_p^* = 5\,^\circ$C (green asterisks), fluor-silanized glass ($\theta_c = 92.2^\circ$) with $T_p^* = 5\,^\circ$C (black filled diamonds), 2 MPa silicone substrate ($\theta_c = 94.3^\circ$) with $T_p^* = 5\,^\circ$C (blue filled squares), 1 MPa silicone substrate ($\theta_c = 95.5^\circ$) with $T_p^* = 5\,^\circ$C (red filled circles), and $T_p^* = 10\,^\circ$C (red empty circles).

In Fig. 5(b), we compare condensation on four different types of substrates with different stiffness and contact angle θ_c, and we also vary the vapour flux Φ by changing the temperature of the cooling plate T_p^*. The porosity of all data falls on a single scaling function when plotted as function of the maximum droplet radius. We interpret this very good, parameter-free data collapse as strong evidence for universality.

Conclusion. We present a series of experiments and simulations where a time-constant uniform water vapour flux condenses on rigid cold surfaces. The emerging droplets patterns undergo four stages on their way to organize into a self-similar arrangement whose number densities feature nonequilibrium scaling (see Fig. 2): (i) a first wave of nucleation of droplets, (ii) uniform growth of roughly equally spaced and monodisperse droplets, (iii) early coalescence, releasing surface area formerly occupied by the first generation of droplets, and (iv) re-population of the gaps between droplets and emergence of a self-similar droplet pattern. In the self-similar regime, the droplet number densities at different times admit a data collapse, Fig. 3. The scaling of the number densities implies a power law decay of the droplet number and the porosity, i.e., the area not covered by droplets. We showed here that substrates with vastly different surface properties evolve towards *identical* power laws with matching exponents and pre-factors, where different surface fluxes are fully accounted for by adopting the maximum droplet radius as a time variable [cf. Eq. (3)]. These findings provide compelling evidence for universal scaling of the asymptotic self-similar regime of breath figures.

Acknowledgments. We would like to express our gratitude to Eric Dufresne, in whose laboratory the present experiments have been performed, for his input and valuable suggestions on how to improve earlier versions of the manuscript. We are thankful to Rob Style, for his help with the design of the experimental setup, and to Kathryn Rosowski and Qin Xu for experimental support. We acknowledge Nicolas Bain, Daniel Dernbach and Robert Haase for insightful discussions, and we thank Martin Callies for feedback on the manuscript. L.S. designed, performed and analyzed the experiments. F.G. and E.A.M. performed the simulations. G.P. and K.S.-M. contributed to the design of experiments and the realization of the samples. L.S. and J.V. developed the theory and wrote the manuscript. All the authors provided feedback on the manuscript. L.S. acknowledges financial support from the Swiss National Science Foundation SNSF (Project No. 192336). K.S.-M. acknowledges financial support by the Swiss National Science Foundation SNSF (Project No. 172827).

[1] Rayleigh, Breath Figures, Nature (London) **86**, 416 (1911).

[2] V. Nikolayev, D. Beysens, A. Gioda, I. Milimouk, E. Katiushin, and J.-P. Morel, Water recovery from dew, J. Hydrology **182**, 19 (1996).

[3] O. Clus, P. Ortega, M. Muselli, I. Milimouk, and D. Beysens, Study of dew water collection in humid tropical islands, J. Hydrol. **361**, 159 (2008).

[4] I. Lekouch, M. Muselli, B. Kabbachi, J. Ouazzani, I. Melnytchouk-Milimouk, and D. Beysens, Dew, fog, and rain as supplementary sources of water in south-western Morocco, Energy **36**, 2257 (2011).

[5] J. W. Rose, Dropwise condensation theory and experiment: A review, Proc. Inst. Mech. Eng. A J. Power Energy **216**, 115 (2002).

[6] R. N. Leach, F. Stevens, S. C. Langford, and J. T. Dickinson, Dropwise condensation: Experiments and simulations of nucleation and growth of water drops in a cooling system, Langmuir **22**, 8864 (2006).

[7] B. S. Sikarwar, N. K. Battoo, S. Khandekar, and K. Muralidhar, Dropwise condensation underneath chemically textured surfaces: Simulation and experiments, J. Heat Transfer **133**, 021501 (2011).

[8] D. Baratian, R. Dey, H. Hoek, D. van den Ende, and F. Mugele, Breath Figures under Electrowetting: Electrically Controlled Evolution of Drop Condensation Patterns, Phys. Rev. Lett. **120**, 214502 (2018).

[9] A. Böker, Y. Lin, K. Chiapperini, R. Horowitz, M. Thompson, V. Carreon, T. Xu, C. Abetz, H. Skaff, A. D. Dinsmore, T. Emrick, and T. P. Russell, Hierarchical nanoparticle assemblies formed by decorating breath figures, Nat. Mater. **3**, 302 (2004).

[10] M. Haupt, S. Miller, R. Sauer, K. Thonke, A. Mourran, and M. Moeller, Breath figures: Self-organizing masks for the fabrication of photonic crystals and dichroic filters, J. Appl. Phys. **96**, 3065 (2004).

[11] Y. Wang, A. S. Özcan, C. Sanborn, K. F. Ludwig, and A. Bhattacharyya, Real-time x-ray studies of gallium nitride nanodot formation by droplet heteroepitaxy, J. Appl. Phys. **102**, 073522 (2007).

[12] K. Rykaczewski, J. Chinn, M. L. Walker, J. H. J. Scott, A. Chinn, and W. Jones, Dynamics of nanoparticle self-assembly into superhydrophobic liquid marbles during water condensation, ACS Nano **5**, 9746 (2011).

[13] S. Feng, Y. Hou, Y. Chen, Y. Xue, Y. Zheng, and L. Jiang, Water-assisted fabrication of porous bead-on-string fibers, J. Mater. Chem. A **1**, 8363 (2013).

[14] L. L. Zhang A., Bai H., Breath figure: A nature-inspired preparation method for ordered porous films, Chem. Rev. **115**, 9801 (2015).

[15] J. Gong, B. Xu, and X. Tao, Three-dimensionally conformal porous microstructured fabrics via breath figures: A nature-inspired approach for novel surface modification of textiles, Sci. Rep. **7**, 2354 (2017).

[16] A. E. Goodling, S. Nagelberg, B. Kaehr, C. H. Meredith, S. I. Cheon, A. P. Saunders, M. Kolle, and L. D. Zarzar, Colouration by total internal reflection and interference at microscale concave interfaces, Nature (London) **566**, 523 (2019).

[17] J. L. Viovy, D. Beysens, and C. M. Knobler, Scaling description for the growth of condensation patterns on surfaces, Phys. Rev. A **37**, 4965 (1988).

[18] F. Family and P. Meakin, Scaling of the Droplet-Size Distribution in Vapor-Deposited Thin Films, Phys. Rev. Lett. **61**, 428 (1988).

[19] F. Family and P. Meakin, Kinetics of droplet growth processes: Simulations, theory, and experiments, Phys. Rev. A **40**, 3836 (1989).

[20] F. Family and P. Meakin, Family and Meakin Reply, Phys. Rev. Lett. **62**, 1700 (1989).

[21] P. Meakin, Steady state droplet coalescence, Phys. A **171**, 1 (1991).

[22] P. Meakin, Droplet deposition growth and coalescence, Rep. Prog. Phys. **55**, 157 (1992).

[23] D. Beysens, A. Steyer, P. Guenoun, D. Fritter, and C. Knobler, How does dew form? Phase Transitions **31**, 219 (1991).

[24] M. Kolb, Scaling of the Droplet-Size Distribution in Vapor-Deposited Thin-Films - Comment, Phys. Rev. Lett. **62**, 1699 (1989).

[25] N. V. Brilliantov, Y. A. Andrienko, P. L. Krapivsky, and J. Kurths, Polydisperse adsorption: Pattern formation kinetics, fractal properties, and transition to order, Phys. Rev. E **58**, 3530 (1998).

[26] J. Blaschke, T. Lapp, B. Hof, and J. Vollmer, Breath figures: Nucleation, growth, coalescence, and the size distribution of droplets, Phys. Rev. Lett. **109**, 068701 (2012).

[27] D. Beysens and C. M. Knobler, Growth of Breath Figures, Phys. Rev. Lett. **57**, 1433 (1986).

[28] G. R. Carlow, R. J. Barel, and M. Zinke-Allmang, Ordering of clusters during late-stage growth on surfaces, Phys. Rev. B **56**, 12519 (1997).

[29] L. Haderbache, R. Garrigos, R. Kofman, E. Sondergard, and P. Cheyssac, Numerical and experimental investigations of the size ordering of nanocrystals, Surf. Sci. **410**, L748 (1998).

[30] S. Ulrich, S. Stoll, and E. Pefferkorn, Computer simulations of homogeneous deposition of liquid droplets, Langmuir **20**, 1763 (2004).

[31] L. Stricker and J. Vollmer, Impact of microphysics on the growth of one-dimensional breath figures, Phys. Rev. E **92**, 042406 (2015).

[32] P. Meakin and F. Family, Scaling in the kinetics of droplet growth and coalescence: Heterogeneous nucleation, J. Phys. A: Math. Gen. **22**, L225 (1988).

[33] J. A. Blackman and S. Brochard, Polydispersity Exponent in Homogeneous Droplet Growth, Phys. Rev. Lett. **84**, 4409 (2000).

[34] M. V. Smoluchowski, Drei Vorträge über Diffusion brownsche molekular Bewegung und Koagulation von Kolloidteichen, Physik. Zeit. **17**, 557 (1916).

[35] D. Fritter, C. M. Knobler, and D. A. Beysens, Experiments and simulation of the growth of droplets on a surface (breath figures), Phys. Rev. A **43**, 2858 (1991).

[36] B. J. Briscoe and K. P. Galvin, Growth with coalescence during condensation, Phys. Rev. A **43**, 1906 (1991).

[37] J. Guadarrama-Cetina and W. González-Viñas, Breath figures of two immiscible substances on a repellent surface, Phys. Rev. E **87**, 054401 (2013).

[38] A. Phadnis and K. Rykaczewski, Dropwise condensation on soft hydrophobic coatings, Langmuir **33**, 12095 (2017).

[39] See Supplemental Material at http://link.aps.org/supplemental/10.1103/PhysRevResearch.4.L012019 for a detailed description of the experimental setup and Monte Carlo simulations, and a full derivation of the scaling laws.

[40] D. T. Gillespie, A general method for numerically simulating the stochastic time evolution of coupled chemical reactions, J. Comput. Phys. **22**, 403 (1976).

[41] C. C. Battaile, The Kinetic Monte Carlo method: Foundation, implementation and application, Comput. Methods Appl. Mech. Engrg. **197**, 3386 (2008).

[42] A. P. J. Jansen, *An Introduction to Kinetic Monte Carlo Simulations of Surface Reactions*, in Lecture notes in Physics Vol. 856 (Springer-Verlag, Heidelberg, 2012), pp. 1–242.

[43] J. Soethoudt, F. Grillo, E. A. Marques, J. R. van Ommen, Y. Tomczak, L. Nyns, S. V. Elshocht, and A. Delabie, Diffusion-mediated growth and size-dependent nanoparticle reactivity during ruthenium atomic layer deposition on dielectric substrates, Adv. Mater. Interf. **5**, 1800870 (2018).

[44] M. Marcos-Martin, D. Beysens, J. Bouchaud, C. Godreche, and I. Yekutieli, Self-diffusion and 'visited' surface in the droplet condensation problem (breath figures), Physica A **214**, 396 (1995).